TECHNICAL PAPER

An advanced modelling to improve the prediction of thermal distribution in friction stir welding (FSW) for difficult to weld materials

Yasin Sarikavak[1]

Abstract

This study explores the thermal distribution of high-strength engineering alloys during the friction stir welding process (FSW). Materials which are difficult to weld or are unweldable by conventional welding processes can be successfully welded by FSW. The specific analysis and modification of the process require an understanding of the actual mechanism of the process. Therefore, a transient, three-dimensional, thermo-mechanical finite element model (FEM) for FSW was developed. The model calculates the temperature distribution during the welding process considering various boundary conditions such as rotational speed, linear speed, normal pressure, tool diameter and material properties. The thermo-mechanical FEM calculations consider the effects of conduction and convection heat transfer. The numerical results are successfully compared and validated by experimental results published in the literature for aluminium alloy, titanium alloy and steel (mild and bainitic) as workpiece materials. The model was found to be useful for understanding the effects of changes in different system parameters, and for selecting the optimum welding conditions before undertaking high-cost physical testing.

Keywords Friction stir welding · Finite element model · Transient thermal model · Heat generation · Temperature distribution

1 Introduction

Friction stir welding (FSW) is a relatively new method which has some advantages over conventional friction welding as well as other welding techniques. The method was invented in The Welding Institute (TWI) in 1991 for joining aluminium alloys which are difficult to weld with conventional methods. Primarily, FSW is applicable for joining low melting point materials such as aluminium alloys, copper and magnesium. The effects of the process parameters on the microstructure [1–3], thermal and mechanical properties of aluminium alloys [4–7] have been studied by several researchers. The feasibility of joining copper and dissimilar materials such as aluminium and copper has also been studied to investigate the optimum machining parameters on

Technical Editor: Izabel Fernanda Machado.

✉ Yasin Sarikavak
sarikavak@gmail.com; ysarikavak@ybu.edu.tr

1   Mechanical Engineering Department, Faculty
of Engineering and Natural Sciences, Ankara Yıldırım
Beyazıt University, 06010 Ankara, Turkey

the mechanical properties of the materials [8, 9]. Recently, several research and development studies have been conducting to explore the potential applications of FSW for harder materials such as steel and titanium alloys [10–17].

The tools used in FSW consist of elements such as shoulder and pin. The shoulder is the material which generates heat, prevents material removal and assists material movement around the tool. The primary function of the pin is to deform the material around the tool and generate heat as a secondary function [18]. The weld strength is primarily dependent on the shoulder diameter whereas the pin diameter has a smaller effect on it [18, 19]. One of the main elements of the welding mechanism in FSW is the heat generated at the interface between workpiece and tool. According to the heat flux, the maximum temperature which is lower than the melting point is observed at the workpiece surface. The increase in temperature makes the workpiece material softer to enable the pin and shoulder to stir the workpiece materials [11]. The temperature variation is the main parameter for controlling the grain growth in microstructure which affects the mechanical properties of a welded workpiece.

Understanding the physical aspects of the FSW process depends on combining an understanding of the joint

formation mechanism, the influence of welding parameters and the properties of the tool and the workpiece materials. Heat generation results from friction and plastic deformation created by the tool and workpiece interaction under various welding conditions. The welding parameters and heat transfer mechanisms which affect the various microstructural zones obtained in FSW are shown in Fig. 1: weld nugget, the thermomechanically affected zone (TMAZ), the heat affected zone (HAZ) and the parent metals are the regions defined after the process [20, 21].

Some finite element models (FEM) are applicable for numerical modelling and a physical understanding of the different parameters in FSW [22, 23] and also for simulating the correlation between these parameters where complex boundary conditions implemented by artificial neural network (ANN) models are available in the literature [24, 25]. Simulating FSW is a complex issue, combining many scientific disciplines [22]. In the literature, there are numerical models simulating the FSW process which are primarily based on the thermal, metallurgical or mechanical aspects [26].

A thermal model was developed for Sc-modified Al–Zn–Mg–Cu alloys joined by FSW under 225, 250, 300 and 400 rpm welding conditions [27]. The thermal model of aluminium alloys presents temperature profiles which incorporate heat generation due to plastic deformation. The predicted temperature profile for Sc-modified Al–Zn–Mg–Cu alloy is in good agreement with the experimental data. Three-dimensional computational fluid dynamics models (CFD) have been developed to predict the temperature distribution via the proposed heat calculations in FSW for dissimilar aluminium alloys such as AA2024 and AA7075 [28, 29]. Several researchers have investigated the temperature distribution during FSW for aluminium alloys based on thermal models with FEM [30]. Su et al. [31] investigated process parameters such as friction coefficient and slip rate which are effective inputs for characterising heat generation at the tool/workpiece interface. Medhi et al. [32] used a tribometer to understand the variations in coefficient of friction between tool steel and aluminium alloy as the workpiece material. The developed FEM enabled investigation of the thermal effect under various welding conditions. Zhang et al. [33] investigated the effect of shoulder size on temperature distribution.

FSW can be applied in many different contexts, such as the aerospace, railway, marine, automotive, pipeline and defence industries [34–36]. Recently, high-strength engineering materials such as titanium alloys and bainitic steels have become promising materials for effective welding using FSW for a variety of engineering structures. High-strength bainitic steels find applications in the railway, pipeline and automotive industries and titanium alloys find applications particularly in the aerospace and biomedical industries [13, 14, 37, 38].

Some developments in the numerical modelling of FSW have been made by researchers for a fundamental understanding of the process, but the majority of the numerical models in the literature have been used to investigate specific individual materials such as aluminium alloys and copper in order to understand the properties of the resulting welded joints. In most of the published numerical modelling studies, the authors performed a limited number of experiments to verify their theoretical findings [30, 39–42]. The experimental findings of other researchers performed in different welding conditions should, however, be used for better comparison and stronger verification of the theoretical findings.

In this current study, therefore, four different materials were used for the simulation studies: mild steel, bainitic steel, aluminium alloy and titanium alloy. A three-dimensional, transient, thermomechanical model was developed to theoretically investigate the effect of rotational speed and the welding speed on temperature distribution. The developed model also considers the axial pressure, the coefficient of friction, heat generation, convection and conduction heat transfers as a boundary condition according to the applied welding parameters. The theoretical findings obtained from the proposed model were validated by experimental findings previously published [11–14] for the different engineering alloys.

2 A thermomechanical model for the FSW process

2.1 Model description

FSW is an efficient solid-state joining process which has many applications in a range of industries. The process involves frictional heating which softens the materials to be

Fig. 1 Microstructure in transverse cross section of the workpiece material after the FSW process: A, parent metal; B, HAZ; C, TMAZ; D, weld nugget [20, 21]
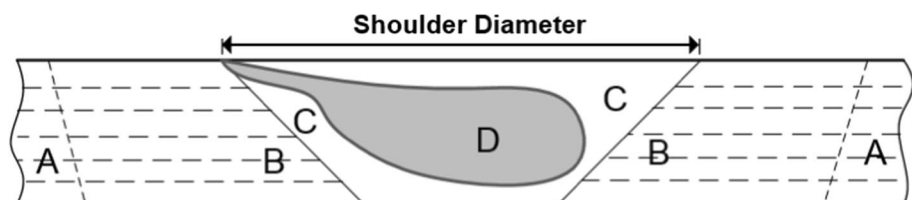
welded and then stirring to mix the materials by a mechanical process. The main mechanism in the FSW process consists of pin and shoulder as tool materials which have contact with the sheet workpiece. The shoulder has a larger diameter and is the main source of heat generated by friction. The shoulder has another function of keeping the material flowing around the tool. The pin has a smaller diameter and is located below the shoulder; its main function is to mix the sheet material to be welded. The sheet materials can be welded using a higher rotation of the tool which increases the heat by friction and causes plastic deformation at the contact area. The process is complex and requires strong thermomechanical knowledge [41]. The three-dimensional model consisted of tool and workpiece material, a rotating tool with a specific diameter, and the application of forward force (see Fig. 2). Horizontal and vertical stirring movements achieve material mixing along the weld line. As the tool moves, heat is generated by the contact friction at the shoulder and workpiece interface and plastic deformation occurs at the stir zone. The properties of the welded materials influence both the geometry of the tool and the workpiece, and the parameters applied during the process.

After forming the three-dimensional model, the FEM simulations started. In this study, the time-dependent (transient) thermal analysis method was selected. The thermal and mechanical material properties of the workpiece and the tool were entered into the simulation module of the model. Each parameter was defined in the model for different materials, as explained in Sect. 3 individually. In FEM, a hexahedral-shaped element was used for meshing the workpiece and the tool. The mesh elements in and near the weld are fine (high mesh density) to enhance the solution accuracy; while the elements far away from the weld are relatively coarse (low mesh density) to save the solution time. Hexahedral-shaped mesh elements are consisting of 935,354 nodes and 207,256 elements for aluminium alloy (AA 2195-T8); 543,515 nodes and 117,820 elements for mild steel (AISI 1018); 161,353 nodes and 32,088 elements for titanium alloy (Ti–6Al–4V); 124,916 nodes and 25,470 elements for bainitic steel plates. After meshing, boundary conditions were entered into the model. Time-dependent thermal heat flow in watts was applied to the shoulder and the shoulder/workpiece interface during the process with the specified linear welding speed on the *x*-axis. Convection heat transfer was defined on the outside diameter of the shoulder and the outer surfaces of the workpiece in contact with the air. The welded plate is considered as a deformable body in the model. The programme formed the mathematical model and generated the solution according to the defined element type, the initial conditions and the boundary conditions. In this study, because of the complex nature of the process, the following assumptions were made to solve the proposed model mathematically: (1) The workpiece is homogeneous and isotropic (2) The heat transfer to the workpiece is by conduction (3) Heat transfer by radiation is neglected (4) The heat transfer coefficients remained constant during the process.

2.2 Heat generation

There was conduction heat transfer along workpiece and tool materials with the heat generated by friction and deformation during the process. The amount of heat conducted along the workpiece and the tool was directly related to the quality of the welding process. For instance, generation of insufficient heat will lead to lower temperatures and the material will not become soft enough at the intersection between tool and workpiece, which might result in the deformation of the tool [11].

Fig. 2 Schematic arrangement of the FSW process in thin plate
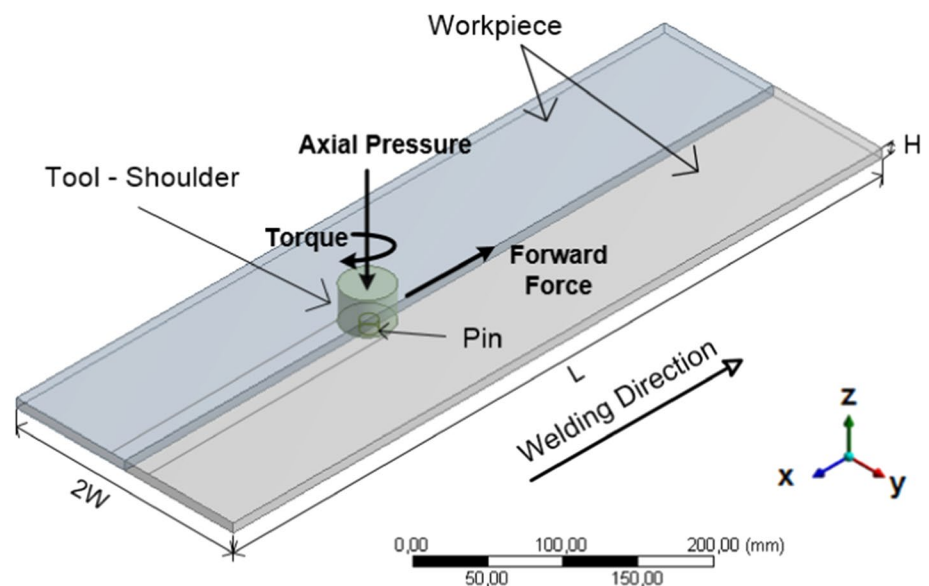
The main generated heat source at the interface between the shoulder and the top of the workpiece is a function of angular velocity (w), friction coefficient (μ), normal pressure and the shoulder diameter. Angular velocity can be expressed in terms of rotational speed (N) at rotation per second [11, 43, 44].

Researchers have suggested various empirical equations for determining the heat generated at the workpiece/tool interface [11, 39, 40, 42]. The ratio of the generated heat from the pin and the shoulder is 0.128 [39, 45]. Under the action of an axial pressure to rotate the tool relative to the plate surface is given in Eq. (1) [39].

$$\int_0^{Mr} dM = \int_0^R \mu P(r) 2\pi r^2 dr = \frac{2}{3}\mu\pi PR^3 \tag{1}$$

where M is the interfacial torque, μ is the friction coefficient, R is the surface radius and P is the pressure distribution. At the workpiece tool interface when all shearing work converted into heat then the heat input per unit area and time calculated according to Eq. (2) [23, 39, 45].

$$Q = \int_0^{M_R} w\,dM = \int_0^R w 2\pi\mu P r^2 dr \tag{2}$$

where Q is the heat generated in watts and w is the angular velocity in rad/s. In Eq. (2), by substituting $w = 2\pi N$; Eq. (3) gives the relation in terms of rotational speed [39].

$$Q = \int_0^R 4\pi^2 \mu PN r^2 dr = \frac{4}{3}\pi^2 \mu PNR^3 \tag{3}$$

where N is the rotational speed and P is the axial pressure across the interface. The energy generated from position R_{i-1} to R_i is defined with Eq. (4) [39].

$$\Delta Q = \frac{4}{3}\pi^2 \mu PN\left(R_i^3 - R_{i-1}^3\right) \tag{4}$$

In this current study, Eqs. (3) and (4) were used for the thermomechanical finite element analysis.

2.3 Axial pressure

The forces applied in the process are another set of parameters which influence the thermal and mechanical phenomena. The axial, welding and transverse forces are the three main forces affecting the process and the axial and welding forces have the major effect on the performance of the joining process. The axial pressure is dependent on axial forces, and rotational speed, welding speed and tool shoulder diameter are the most significant parameters affecting axial force and the heat input values in the FSW process [46]. Several empirical models have been developed to describe the axial forces as a function of welding conditions [47].

2.4 Heat transfer model

A schematic representation of the heat transfer model of a workpiece in the FSW process is given in Fig. 3. The energy balance during the process is given in Eq. (5). Here, Q is the heat flux generated from the friction between the workpiece and the tool. Because of the existence of air around the shoulder/workpiece interface, there is convection heat transfer; q_1 is the heat loss from the upper surface of the workpiece to the environment via convection heat transfer and q_2 is the conducted heat from the bottom surface of the workpiece which has an interface with the equipment; q is

Fig. 3 Heat transfer model of the workpiece in FSW
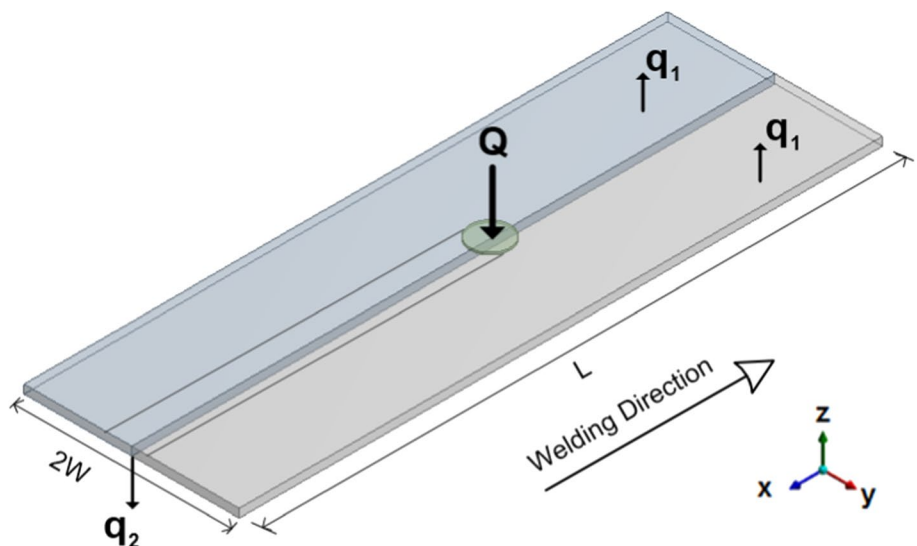
the heat absorbed in the workpiece during the process and varies over time as the system has a transient nature [11].

$$Q = q_1 + q_2 + q \tag{5}$$

The shoulder and pin move over the workpiece along the x-axis at a velocity of V_x. The three-dimensional partial differential equation for heat conduction in the workpiece is given in Eq. (6) and expressed as follows: [39, 43]

$$\rho c \left(\frac{\partial T}{\partial t} + V_x \frac{\partial T}{\partial x} \right) = \frac{\partial}{\partial x} \left(k_x \frac{\partial T}{\partial x} \right) + \frac{\partial}{\partial y} \left(k_y \frac{\partial T}{\partial y} \right) + \frac{\partial}{\partial z} \left(k_z \frac{\partial T}{\partial z} \right) \tag{6}$$

where T is the temperature, c is the specific heat, ρ is the density, k_x, k_y, k_z are the heat conductivities along the x, y and z directions and V_x is the welding speed. The conduction and convection heat transfer coefficients for various workpiece materials are the other important parameters for determining the thermomechanical properties in FSW. The initial boundary condition in the system is expressed as follows:

$$T(x, y, z, t) = T_0 \tag{7}$$

where in Eq. (7), T_0 is the initial temperature (equal to the ambient temperature). Because of the existence of heat flow between tool and workpiece, the boundary conditions of the shoulder radius are given in Eq. (8).

$$k \frac{\partial T}{\partial n} = Q \tag{8}$$

where n is the normal of the surface, k is the thermal conductivity coefficient and Q is the heat generated by friction and deformation during the FSW process. In Eq. (9), outside the tool and shoulder radius, convective heat transfer is defined for the workpiece surfaces exposed to air. The convective heat transfer equation is expressed as follows:

$$k \frac{\partial T}{\partial n} = h(T - T_0) \tag{9}$$

where h is the convective heat transfer coefficient between workpiece and air, and taken as 5 W/m^2 °C for FEM calculations [11].

3 Materials and experimental procedure

In this study, the experimental results of four different published studies [11–14] were used to check the validity of the proposed model. Chao et al. [11] used 8.13-mm-thick

Table 1 Thermal properties of AA 2195-T8 [11]

Temperature (°C)	Thermal conductivity (W/m °C)	Specific heat (J/kg °C)
0	85	890
50	100	930
100	110	970
150	118	1010
200	125	1050
250	130	1070
300	138	1080

aluminium alloy as the workpiece material. The AA2195-T8 plates had a density of 3 g/cm^3. The yield and ultimate tensile strengths were 570 MPa and 600 MPa, respectively. The thermal and chemical properties of AA2195-T8 are given in Tables 1 and 2, respectively [11].

The FSW experiments were conducted at 240 rpm rotational speed and 3.32 mm/s linear welding speed (cold weld). Heat input to the workpiece during the welding process was at 1860 W. Transient heat transfers existed in both the workpiece and the tool material. M2 tool steel that has rectangular grooves was used as the tool and the heat flux in the tool was a function of the dynamic friction coefficient, the downward force acting on the workpiece, the temperature and the contact surface conditions. The welding tool had a shoulder diameter of 25.4 mm, a pin radius of 5 mm and a 8-mm pin length [11]. In dry conditions, the friction coefficient between aluminium and steel ranges 0.47–0.61. Here, it was taken as 0.61 for the FEM calculations. In the experiment, thermocouples were installed at depths of 2 mm and 4 mm and to the bottom of the workpiece. The locations of the thermocouples along the y-axis were at 5, 12.7 and 25.4 mm from the weld line [11].

Nandan et al. [12] used AISI 1018 steel plates with a density of 7860 kg/m^3 for their experiment. The plates were 410 mm in length, 78 mm in half-width and 6.35 mm in thickness. The cylindrical shoulder diameter was 19 mm, the pin radius was 3.95 mm, and the pin length was 6.22 mm. The cylindrical pin was threaded with a pitch of 1 mm. The chemical composition of AISI 1018 Mn steel contains 0.18% C, 0.82% Mn, 0.011% P, 0.006% S and less than 0.01% Si. The thermophysical property of the steel is given in Table 3. Temperature profiles were obtained at 450 rpm rotational speed, 0.42 mm/s welding speed and 65.9 MPa axial pressures. The friction coefficient for the centre of the radial axis

Table 2 Chemical composition of AA 2195-T8 (% mass) [11]

Material	Mn	Si	Fe	Al	Cu	Li	Mg	Ag	Zn	Zr	Ti
AA2195-T8	0–0.25	0–0.12	0–0.15	91.9–94.9 Bal.	3.7–4.3	0.8–1.2	0.25–0.8	0.25–0.6	0–0.25	0.080–0.16	0–0.1

Table 3 Thermal properties of AISI 1018 mild steel [12]

Temperature (K)	Thermal conductivity (W/mK)	Specific heat (J/kgK)
400	51	480
600	45	560
800	37	700
1000	28	880
1200	26	1100

Table 4 Chemical composition of Ti–6Al–4V (% mass) [13]

Material	C	O	N	Fe	Al	V	Y	Ti
Ti–6Al–4V	0.019	0.14	0.009	0.18	6.2	3.87	< 50 ppm	Bal.

Table 5 Thermal properties of Ti–6Al–4V [13]

Temperature (°C)	Thermal conductivity (W/mK)	Temperature (°C)	Specific heat (J/gK)
20	6.6	20	0.580
315	10.6	425	0.670
		870	0.930

of the mild steel ranges from 0.2 to 0.4; in this experiment, it was taken as 0.4 for the FEM calculations. The experimental temperature values were collected 3 mm below the workpiece surface at distances of 4, 8 and 12 mm along the y-axis from the weld line.

Tungsten tools with a density of 19,400 kg/m^3 were used for the experiment. During the process, the heat input to the workpiece was calculated at 2228 W and used as input data for the FEM calculations. Heat transfer from the bottom surface of the workpiece was taken as 50 W/m^2 K [12].

Kitamura et al. [13] used titanium alloys (Ti–6Al–4V) (300 mm × 35 mm × 2 mm) as workpiece materials; the chemical composition, specific heat and thermal conductivity values used for the FEM calculations are given in Tables 4 and 5. Ti–6Al–4V has a 4420 kg/m^3 density, 950 MPa tensile strength, 113.8 GPa elasticity modulus and 0.342 Poisson ratio.

A tungsten carbide (WC)-based alloy was used as the tool material with a shoulder diameter of 15 mm, pin radius of 3 mm and 1.8 mm pin length [13]. The thermal conductivity of the tool material was 95 W/mK [48]. The friction coefficient between titanium alloy and tungsten carbide ranges from 0.25 to 0.42 under dry conditions [49]. In this current study, the friction coefficient was taken as 0.42 for the FEM calculations. The calculated heat inputs for 25 mm/min linear welding speed were 698.8, 814.8, 930.8 W at 300, 350 and 400 rpm rotational speeds, respectively. At a 1000 rpm rotational speed and 400 mm/min linear welding speed, the calculated heat input was 2328 W. In the experiment, the temperature change during the process was measured by the thermocouples located at the bottom of the workpiece [13].

Ramakrishna et al. [14] investigated the weldability of ultrafine bainitic steel plates with 3 mm thickness. A polycrystalline cubic boron nitride (PcBN) tool was used in their experiment with a constant transverse speed of 35 mm/min under various rotational speeds. Tool material has a shoulder diameter of 15 mm, pin radius of 3 mm and a pin length of 2.8 mm. Tools were tilted by 2 degrees from the plate normal. The density and thermal conductivity of the tool were 3.8 g/cm^3 and 120 W/mK, respectively [50–52]. The specific heat of PcBN is 700 J/kg °C [51]. Experimental thermography analysis was conducted between the tool/workpiece interface in various welding conditions. The thermal conductivity and specific heat of the workpiece material were taken as 44.5 W/mK and 0.475 J/g °C, respectively, for the finite element analysis (FEA) calculations. Ultrafine bainitic steel has a 1370 MPa ultimate tensile strength and its chemical composition is given in Table 6 [14, 53].

In the literature, the friction coefficient of cubic boron nitride and steel ranges from 0.38 to 0.5 [54]. In this current study, the friction coefficient was taken as 0.5 for the FEA calculations. The calculated heat inputs were 243, 303.2, 456.8 and 608.5 W at rotational speeds of 80, 100, 150 and 200 rpm, respectively. The main properties of the workpiece materials and the boundary conditions used for the FEA are summarised in Table 7.

4 Results and discussion

4.1 Comparison of the theoretical and experimental results of aluminium alloy (AA2195-T8)

The developed model enabled the temperature profiles in various regions of the workpiece material, including the

Table 6 Chemical composition of ultrafine bainitic steel (% mass) [14]

Material	C	Mn	Si	Cr	Fe	Al	Ti
Bainitic steel	0.34	1.80	1.51	0.92	Bal.	0.015	0.032

Table 7 Workpiece material properties and the welding conditions

| Material	Density (kg/m³)	Ultimate Tensile Strength (MPa)	Length (L) (mm)	Half-width (W) (mm)	Thickness (H) (mm)	Shoulder diameter (mm)	Axial pressure (P_T) (MPa)	Heat transfer coeff. (top) (W/m²C)	Heat transfer coeff. (bottom)(W/m²K)	Rotational speed (rpm)	Linear welding speed (mm/min)
Aluminium alloy AA2195-T8 [11]	3000	600	610	102	8.13	25.4	13	5	350	240	199.2
Mild steel AISI1018 [12]	7860	440	410	78	6.35	19	65.9	5	50	450	25.2
Titanium alloy Ti–6Al–4V [13]	4420	950	300	35	2	15	60 [10]	5	–	300 / 350 / 400 / 400 / 400 / 1000	25 / 25 / 25 / 50 / 100 / 400
Bainitic steel [14]	7860 [12]	1370	200	30	3	15	65.9	5	–	80 / 100 / 150 / 200	35 / 35 / 35 / 35
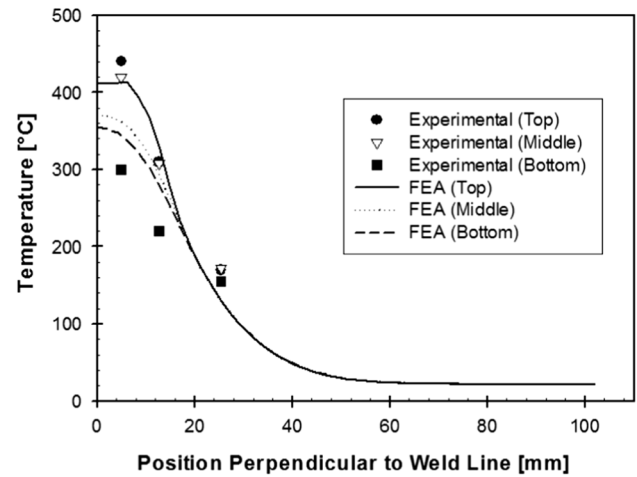
Fig. 4 Experimental [11] and FEA results of temperature distribution for the top, middle and bottom of the AA2195-T8 work piece along the y-axis

weld line, to be obtained. It was therefore possible to determine the maximum temperature according to time. In the experiment [11], AA2195-T8 plates were joined using the FSW process at a 300 rpm rotational speed and 199.2 mm/min linear welding speed. Thermocouples were installed at three different locations on the workpiece material named 'top' (2 mm below the workpiece surface), 'middle' (4 mm below the workpiece surface) and 'bottom' (8.13 mm below the workpiece surface). The experimental and FEA results of the temperature profiles in the same welding conditions are shown in Fig. 4.

Theoretical results closer to the experimental ones were obtained for the maximum temperature values. The experimental and theoretically calculated results of the temperature profiles were very consistent, especially for the values at a distance of 12.7 mm from the weld line along the y-axis. The experimentally measured temperature values were 310, 308 and 220 °C and the calculated theoretical values were 330, 292 and 279 °C at the top, middle and bottom locations, respectively, for the AA2195-T8 plate at the 12.7 mm location. At the distance of 5 mm from the weld line, the experimentally measured maximum temperatures were 440, 420 and 300 °C, and the theoretically calculated values were 417, 360 and 340 °C at the top, middle and bottom locations, respectively. The majority of the theoretical results were therefore very consistent with the experimental ones. However, the values obtained from the FEA were lower than the experimental ones at the distance of 25.4 mm from the weld line. The measured values were 170, 172 and 155 °C, and the theoretically investigated values were 130, 129 and 129 °C at the top, middle and bottom locations, respectively. This indicates that at the corner and on the outside of the shoulder diameter, the convective heat transfer conditions

were the most effective parameters for temperature distribution and should be entered into the model considering environmental conditions for obtaining exact solutions for the whole system.

4.2 Comparison of the theoretical and experimental results of mild steel (AISI 1018)

AISI 1018 steel with a 6.35 mm thickness was welded with a rotational speed of 450 rpm and a 25.2 mm/min linear weld speed. The model was in good agreement with the validated results in the literature [12] (*see* Fig. 5). The experimentally obtained temperature values at distances of 4, 8 and 12 mm from the centreline of the weld were 1180, 1160 and 880 K, respectively, and the theoretically obtained values were 1090, 1060 and 710 K. The change rate in the temperature distribution along the y-axis was therefore consistent with the results of the experimental work.

4.3 Comparison of the theoretical and experimental results of titanium alloy (Ti–6Al–4V)

Ti–6Al–4V alloys with a 2-mm thickness were joined under various welding conditions. The experimental work conducted for the conditions of both rotational speed and weld speed remained constant. Figure 6 shows the FEA and experimental results of Ref. [13]. The experimental and theoretical findings were very consistent, especially at the constant rotational speed of 400 rpm. At 400 rpm under various weld speeds, namely 25, 50 and 100 mm/min, the experimental values were 990, 970 and 965 °C, and the theoretical values were 953, 935 and 853 °C, respectively. The developed model was therefore highly sensitive to weld speed. However, at lower rotational speeds such as 300 rpm,
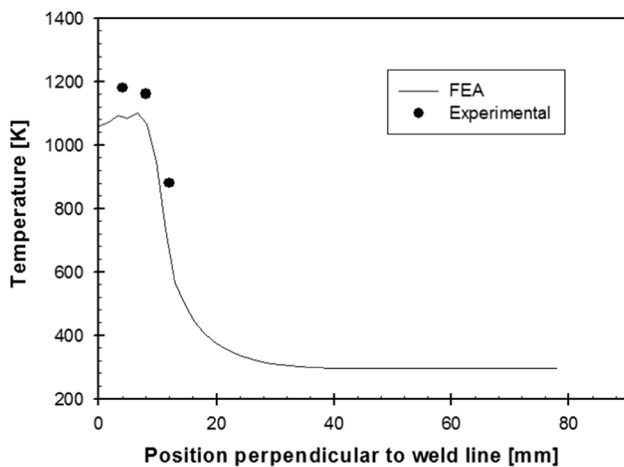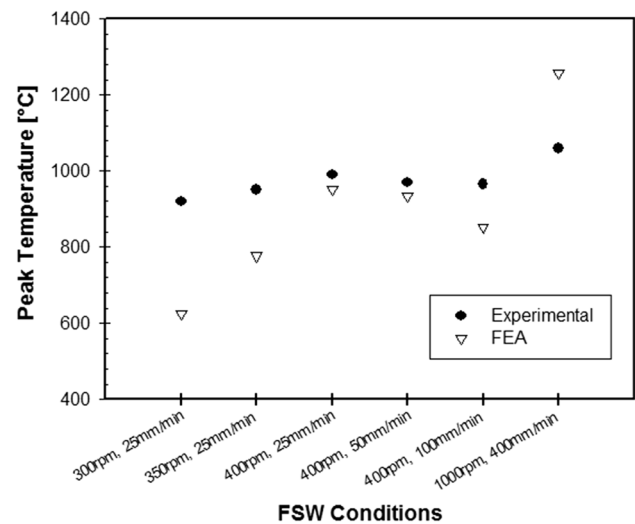
Fig. 6 Experimental [13] and FEA results of peak temperature for various FSW conditions of titanium alloy

the FEA result was lower than the experimental value. At higher rotational speeds such as 1000 rpm, the FEA result was higher than the experimental one.

In the weld line with the plastic deformation, the grains are refined and in the TMAZ and HAZ, deformation and continuous dynamic recrystallization processes have influence on the temperature profiles in the workpiece material [16]. It is expected that higher rotational speed result with larger grained weld microstructure and conversely lower rotational speed expected to produce fine grained microstructures [55]. For the tested parameters of Edwards and Ramulu's study [55]; 400 rpm rotational speed resulted with the largest grained weld microstructure however 200 rpm rotational speed had the smallest grain size qualitatively for Ti–6Al–4V as a workpiece material. Zhou et al. [56] concluded that highest temperature obtained at the stir zone and optimum defect free welds obtained where significantly refined microstructure was developed in the stir zone because of the combined effect of the dynamic recrystallization and phase transformation under 400 rpm rotational speed with 50 mm/min welding speed for 2-mm-thick Ti–6Al–4V workpiece. Similarly, in Fig. 8b at 400 rpm and 50 mm/min welding parameters, finite element model results show the maximum temperature in the stir zone as observed in the experimental work [56]. In Fig. 6, very consistent results obtained for the experimental study and finite element analysis for 400 rpm rotational speeds with various welding speed similar like the study conducted by Zhou et al. [56]. However, for the rotational speeds of 300 rpm, 350 rpm and 1000 rpm with the change in microstructure, grain size and its effect on thermal properties and cooling rates; relatively low (for 300 rpm and 350 rpm) and relatively high (for 1000 rpm) peak temperatures observed at

Fig. 5 Experimental [12] and FEA results of temperature distribution for the mild steel along the y-axis

the finite element analysis results. Thus, according to rotational speed (for low and high rpm values), grain size, grain morphology and change in physical properties in the actual mechanism has an influence on the temperature profile. A correlation between these parameters should be studied in the future work for better understanding of the phenomena. However, temperature profile calculated at the present thermomechanical finite element model gives useful and consistent results with the experimental ones that can help to understand the change according to temperature distribution and to clarify optimum welding parameters.

Figures 7 and 8 show comparisons of the temperature profiles of the FEA results under various welding conditions along the y–z plane. In Fig. 7a, at 300 rpm, the maximum temperature was obtained outside the diameter of the tool. In Fig. 7b, c, however, more homogenous temperature

profiles were observed, and the maximum temperatures were obtained at the centre of the weld line. The analyses indicate that temperature values decrease moving radially outward from the centre of the weld line.

According to the weld direction and tool rotation, an asymmetry exists in heat transfer and temperature distribution in the welded plates [12, 16, 57]. Advancing side is called the half plate in which the direction of the tool rotation is same as the direction of the welding and the opposite is called the retreating side. In the literature results [12, 16] advancing side experience higher temperatures than in comparison to the retreating side. For the previously reported experimental work of FSW for Ti–6Al–4V alloy; typical temperature distribution at the top of the workpiece for advancing and retreating side measured as 546 °C and 531 °C, respectively [16, 20].
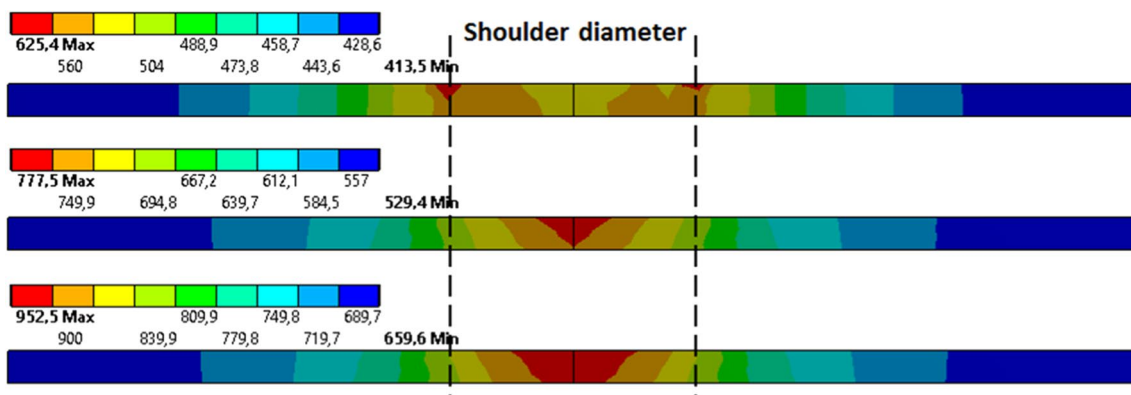

Fig. 7 Effect of rotational speed on temperature (°C) of a Ti–6Al–4V workpiece along the y–z plane: **a** 300 rpm, 25 mm/min **b** 350 rpm, 25 mm/min **c** 400 rpm, 25 mm/min
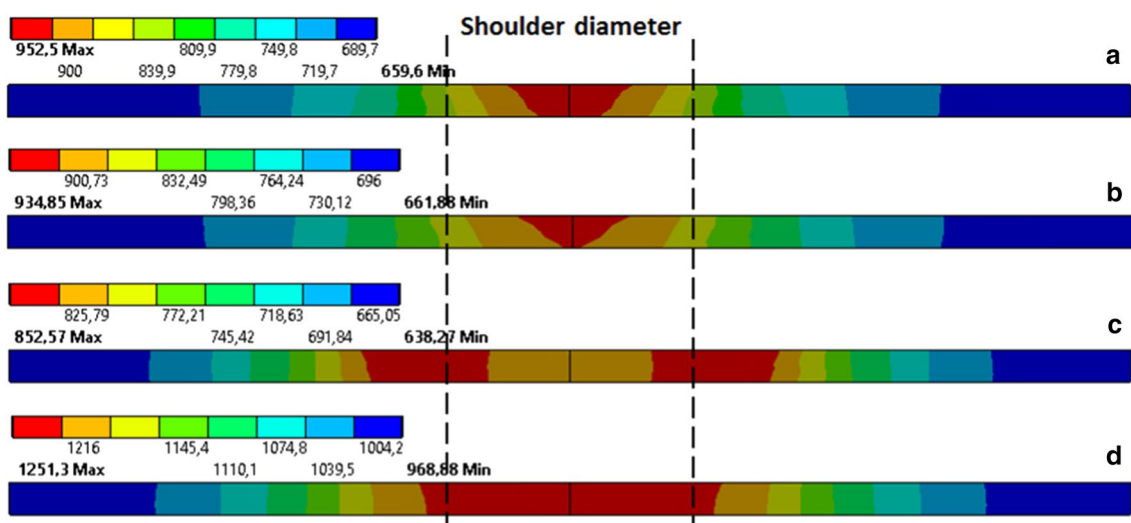

Fig. 8 Effect of linear welding speed on temperature (°C) of the Ti–6Al–4V workpiece along the y–z plane: **a** 400 rpm, 25 mm/min **b** 400 rpm, 50 mm/min **c** 400 rpm, 100 mm/min **d** 1000 rpm, 400 mm/min

In Fig. 7a at the top of the workpiece 625 °C and 580 °C; in Fig. 7b 685 °C and 675 °C; in Fig. 7c 840 °C and 835 °C, maximum temperatures obtained at the outside diameter of the shoulder (7.5 mm apart from the weld centre) for advancing and retreating side, respectively.

In Fig. 8a, b, d, the maximum temperatures observed at the centre of the weld line are shown. In Fig. 8c, when the travel speed of the tool increased to 100 mm/min, the maximum temperature was obtained at the outside diameter of the shoulder. This analysis shows that an increase in weld speed results in changes in the temperature profiles and the maximum temperatures occur at a location radially outward from the centre of the weld line. With increasing welding parameters to 1000 rpm and 400 mm/min, the workpiece material reached 1251 °C, which is close to the melting temperature of Ti–6Al–4V, and the maximum temperature was obtained at the centre of the weld line. Temperature distribution affects the quality of the welding process and the model gave beneficial results for selecting the optimum welding conditions in terms of homogenous temperature distribution to soften the different materials.

A similar tendency has been already obtained as in Fig. 8a as at the top of the workpiece 840 °C and 835 °C; in Fig. 8b 852 °C and 847 °C; in Fig. 8c 839 °C and 833 °C; in Fig. 8d 1233 °C and 1230 °C maximum temperatures obtained at the outside diameter of the shoulder for advancing and retreating side, respectively. As expected, advancing side experience higher temperatures than the retreating side.

4.4 Comparison of the theoretical and experimental results of bainitic steel

Bainitic steel plates of a 3-mm thickness were welded at a 35 mm/min weld speed and 80, 100, 150 and 200 rpm rotational speeds. The experimental [14] and theoretical results for the peak temperature were very consistent, especially at 80 and 100 rpm rotational speeds under the same weld speed (*see* Fig. 9). With an increase in the rotational speed, the experimental values became smaller than the theoretical ones. In the FEA stage of this study, heat input according to friction and deformation was calculated using friction coefficient, surface radius, axial pressure and rotational speed. The findings showed a linear increase in temperature according to the defined dependent parameters. However, during the actual joining process for hard and high-strength materials such as bainitic steels, the temperature changes according to friction and the stir process did not show linear and stable characteristics. The thermography profile at the stir zone below the interface of the experimental work showed dramatic changes during the actual process [14]. Thus, the theoretical values were slightly higher than the experimental ones at 150 and 200 rpm rotational speeds, but the developed
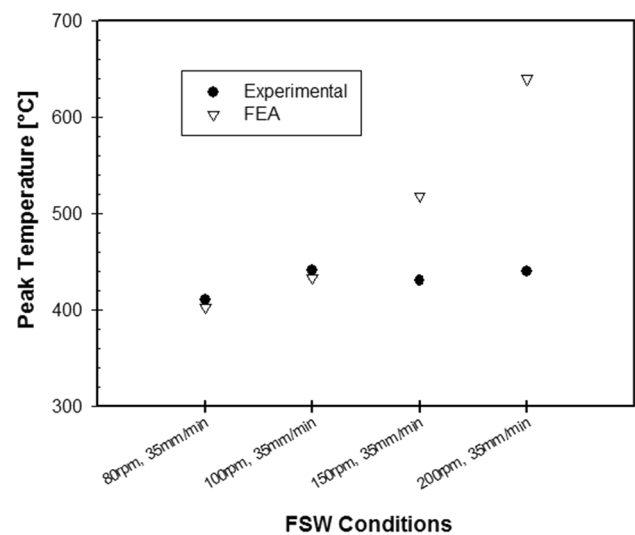

Fig. 9 Experimental [14] and FEA results of peak temperature for various FSW conditions of bainitic steel

model is useful for understanding the optimal welding conditions for bainitic steels.

In the experimental study for ultrafine bainitic steels (transformation induced plasticity-TRIP steels) microstructures were investigated at all rotational speeds across the cross section in the cited Ref. [14]. Temperature data collected at stir zone where the microstructure and hardness vary as a function of rotational speed. In stir zone, the retained austenite content decreased with increasing rotational speed. Also increase in rotational speed results with increase in hardness at the stir zone. It is stated that higher hardness could be associated with the transformation products such as retained austenite and high dislocation density [14]. Cortes et al. [58] reported the effect of retained austenite on the thermal/electrical properties of five advanced high-strength TRIP steels. The physical properties of TRIP steels are influenced by the presence and quantity of impure atoms and precipitated phases. In steels heat is transferred via migration of free electrons. At higher temperature regions, free electrons with higher kinetic energy travel to lower temperature regions until it collides with an imperfection or a phonon in the material. Thus, any imperfection such as retained austenite has a direct impact on thermal conductivity and electrical resistivity that are the dominant parameters for calculation of the temperature profiles [58]. The presented model in this study consistent with experimental result at 80 and 100 rpm rotational speeds. Increase in rotational speed results with increase in hardness, change in microstructure and quantities of transformation products that leads differences in physical properties. Also ultrafine bainitic steel have excellent combination of tensile strength, hardness

and elongation where 1370 MPa, 750 HV and 21% elongation obtained in the 3 mm thick plates respectively [14]. These superior mechanical properties cause complex and unstable deformation at elevated rotational speeds during the solid-state welding process. Thus, relatively higher peak temperatures obtained in FEA than the experimental results for the rotational speeds i.e. 150 and 200 rpm.

Temperature profiles of a 3-mm-thick bainitic steel workpiece at various rotational speeds along the y–z plane is seen in Fig. 10. The peak temperatures were observed at the centre of the weld for all welding conditions. At a 35 mm/min weld speed and 80 rpm rotational speed, the maximum temperature reached 403 °C at the centre of the weld line. The temperature gradually decreased at a distance of shoulder radius from the weld line along the y-axis. With an increase in rotational speed, the temperature values at the centre of the weld line increased. The investigated maximum temperatures were 433, 518 and 640 °C at 100, 150 and 200 rpm rotational speeds, respectively.

In Fig. 10a at the top of the workpiece 398 °C and 396 °C; in Fig. 10b 428 °C and 426 °C; in Fig. 10c 512 °C and 510 °C and; in Fig. 10d 633 °C and 630 °C maximum temperatures obtained at the outside diameter of the shoulder (7.5 mm apart from the weld centre) for advancing and retreating side respectively. Similarly advancing side experience higher temperatures than retreating side however relatively less difference obtained when compared with Ti–6Al–4V alloy.

The welding parameters and the temperature results obtained from the developed thermomechanical model of the four different materials examined in this study are summarised in Table 8. The temperature mapping shows that the peak temperatures were mainly located at the stir zones and at the top surface of the workpiece materials. Through the thickness of the workpiece, the temperature gradually decreased. The highest temperature difference through thickness was investigated at 6.35-mm-thick mild steel where the calculated value was 385 °C. For the bainitic steel workpiece, the peak temperature increased with an increase in rotational speed, but the temperature difference through the thickness remained constant (5 °C).

5 Conclusion

A time-dependent, three-dimensional, thermomechanical model of the FSW process was developed in order to understand the temperature profiles of various engineering materials such as steel, aluminium alloy and titanium alloy. The model included several primary aspects of the FSW process such as rotational speed, shoulder diameter, linear welding speed, axial pressure, coefficient of friction, heat generation, and convection and conduction heat transfer. The temperature distribution around the weld line obtained from the developed model was compared with the experimental values reported in the literature.

The theoretical predictions and the experimental results showed that the maximum temperature gradients on the y- and z-axes were located at the outside diameter of the
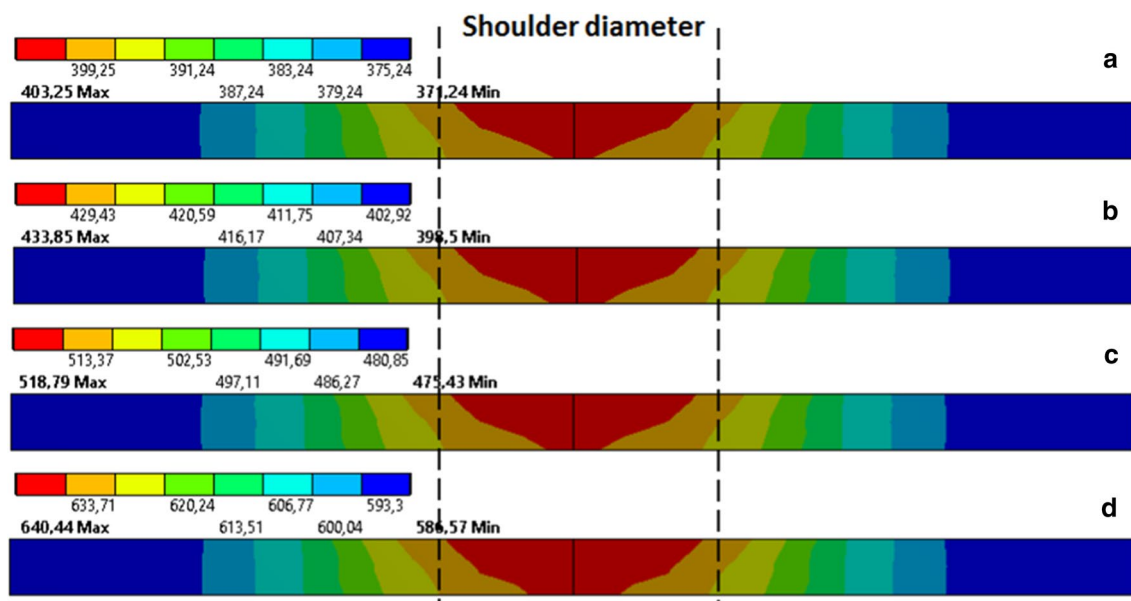

Fig. 10 Effect of rotational speed on temperature (°C) of high-strength bainitic steel workpiece along the y–z plane with a 35 mm/min weld speed: **a** 80 rpm, **b** 100 rpm, **c** 150 rpm, **d** 200 rpm

Table 8 Temperature difference for workpiece materials under various FSW conditions

Material	Thickness (mm)	Shoulder diameter (mm)	Rotational speed (rpm)	Travel (mm/min)	Peak temperature (°C)	Temperature difference (through thickness) (°C)
Aluminium alloy AA2195-T8	8.13	25.4	240	199.2	417	63
Mild steel AISI1018	6.35	19	450	25.2	828	385
Titanium alloy Ti–6Al–4V	2	15	300	25	625	87
			350	25	777	30
			400	25	952	35
			400	50	935	31
			400	100	852	14
			1000	400	1251	1
Bainitic steel	3	15	80	35	403	4
			100	35	434	5
			150	35	519	5
			200	35	640	5

shoulder radius or at the centre of the weld line according to the boundary conditions applied in the welding process.

Increases in rotational speed resulted in increases in peak temperature in the workpiece. Welding speed had a significant influence on the temperature profile. An increase in weld speed resulted in a decrease in peak temperature. For titanium alloys, at 400 rpm, 100 °C temperature difference was obtained at 25 mm/min and 100 mm/min linear weld speeds.

The location of peak temperature ranged according to the travel and rotational speeds. The thickness of the plates effects heat transfer and the observed temperature through the thickness. The homogenous temperature distribution that soften the material at stir zone, improves the weld ability of the workpiece materials.

The developed model successfully predicted the peak welding temperature and the temperature distributions for different welding parameters of the FSW process. The model was in good agreement with the experimental results published in the literature and capable of providing good estimates for various engineering alloys. The effects of welding speed and tool rotational speed were individually investigated for high-strength materials, namely titanium alloy and bainitic steel. The model was found to be useful for understanding the effects of changes in different system parameters, and for selecting the optimum welding conditions before undertaking high-cost physical testing.

Compliance with ethical standards

References

1. Mahoney MW, Rhodes CG, Flintoff JG et al (1998) Properties of friction-stir-welded 7075 T651 aluminum. Met Mater Trans A 29:1955–1964. https://doi.org/10.1007/s11661-998-0021-5
2. Rhodes CG, Mahoney MW, Bingel WH et al (1997) Effects of friction stir welding on microstructure of 7075 aluminum. Scr Mater 36:69–75. https://doi.org/10.1016/S1359-6462(96)00344-2
3. Do Vale NL, Torres EA, de Santos TFA et al (2018) Effect of the energy input on the microstructure and mechanical behavior of AA2024-T351 joint produced by friction stir welding. J Braz Soc Mech Sci Eng 40:467. https://doi.org/10.1007/s40430-018-1372-5
4. Patil S, Tay YY, Baratzadeh F, Lankarani H (2018) Modeling of friction-stir butt-welds and its application in automotive bumper impact performance Part 1. Thermo-mechanical weld process modeling. J Mech Sci Technol 32:2569–2575. https://doi.org/10.1007/s12206-018-0514-0
5. Altenkirch J, Steuwer A, Peel M et al (2008) The effect of tensioning and sectioning on residual stresses in aluminium AA7749 friction stir welds. Mater Sci Eng A 488:16–24. https://doi.org/10.1016/j.msea.2007.10.055
6. Leonard AJ, Shercliff HR, Withers PJ (2009) Friction stir welding of aluminium alloys. Int Mater Rev 54:49–93. https://doi.org/10.1179/174328009X411136
7. Rao KV (2018) Evaluation of welding characteristics using three-dimensional finite element simulation and experimentation for FSW of aluminum 6061. J Braz Soc Mech Sci Eng 40:86. https://doi.org/10.1007/s40430-018-0963-5
8. Lee WB, Jung SB (2004) The joint properties of copper by friction stir welding. Mater Lett 58:1041–1046. https://doi.org/10.1016/j.matlet.2003.08.014
9. Eslami N, Harms A, Henke B et al (2019) Electrical and mechanical properties of friction stir welded Al–Cu butt joints. Weld World 63:903–911. https://doi.org/10.1007/s40194-019-00719-y

10. Nandan R, Lienert TJ, DebRoy T (2008) Toward reliable calculations of heat and plastic flow during friction stir welding of Ti–6Al–4V alloy. Int J Mater Res 99:434–444. https://doi.org/10.3139/146.101655

11. Chao YJ, Qi X, Tang W (2003) Heat transfer in friction stir welding: experimental and numerical studies. J Manuf Sci Eng 125:138–145. https://doi.org/10.1115/1.1537741

12. Nandan R, Roy GG, Lienert TJ, Debroy T (2007) Three-dimensional heat and material flow during friction stir welding of mild steel. Acta Mater 55:883–895. https://doi.org/10.1016/j.actamat.2006.09.009

13. Kitamura K, Fujii H, Iwata Y et al (2013) Flexible control of the microstructure and mechanical properties of friction stir welded Ti–6Al–4V joints. Mater Des 46:348–354. https://doi.org/10.1016/j.matdes.2012.10.051

14. Ramakrishna RVSM, Sankara Rao KB, Reddy GM, Gautam JP (2018) Friction stir welding of advanced high strength (bainitic) steels for automotive applications. Mater Today Proc 5:17139–17146. https://doi.org/10.1016/j.matpr.2018.04.122

15. Çam G, İpekoğlu G, Küçükömeroğlu T, Aktarer SM (2017) Applicability of friction stir welding to steels. J Achiev Mater Manuf Eng 80:65–85. https://doi.org/10.5604/01.3001.0010.2027

16. Gangwar K, Ramulu M (2018) Friction stir welding of titanium alloys: a review. Mater Des 141:230–255. https://doi.org/10.1016/j.matdes.2017.12.033

17. Bhadeshia HKDH, Debroy T (2009) Critical assessment: friction stir welding of steels. Sci Technol Weld Join 14:193–196. https://doi.org/10.1179/136217109X421300

18. Colegrove PA (2003) Modelling of friction stir welding by Paul Andrew Colegrove. University of Cambridge, Cambridge

19. Tang W, Guo X, McClure JC et al (1998) Heat input and temperature distribution in friction stir welding. J Mater Process Manuf Sci 7:163–172. https://doi.org/10.1106/55TF-PF2G-JBH2-1Q2B

20. Mishra RS, Mahoney MW (2007) Friction stir welding and processing. ASM Int, Ohio

21. Dong P, Lu F, Hong JK, Cao Z (2013) Coupled thermomechanical analysis of friction stir welding process using simplified models. Sci Technol Weld Join 6:281–287. https://doi.org/10.1179/136217101101538884

22. He X, Gu F, Ball A (2014) Progress in materials science a review of numerical analysis of friction stir welding. Prog Mater Sci 65:1–66. https://doi.org/10.1016/j.pmatsci.2014.03.003

23. Neto DM, Neto P (2013) Numerical modeling of friction stir welding process: a literature review. Int J Adv Manuf Technol 65:115–126. https://doi.org/10.1007/s00170-012-4154-8

24. Okuyucu H, Kurt A, Arcaklioglu E (2007) Artificial neural network application to the friction stir welding of aluminum plates. Mater Des 28:78–84. https://doi.org/10.1016/j.matdes.2005.06.003

25. Krishnan MM, Maniraj J, Deepak R, Anganan K (2018) Prediction of optimum welding parameters for FSW of aluminium alloys AA6063 and A319 using RSM and ANN. Mater Today Proc 5:716–723. https://doi.org/10.1016/j.matpr.2017.11.138

26. Bastier A, Maitournam MH, Roger F, Van KD (2008) Modelling of the residual state of friction stir welded plates. J Mater Process Technol 200:25–37. https://doi.org/10.1016/j.jmatprotec.2007.10.083

27. Hamilton C, Sommers A, Dymek S (2009) A thermal model of friction stir welding applied to Sc-modified Al–Zn–Mg–Cu alloy extrusions. Int J Mach Tools Manuf 49:230–238. https://doi.org/10.1016/j.ijmachtools.2008.11.004

28. Tang J, Shen Y (2016) Numerical simulation and experimental investigation of friction stir lap welding between aluminum alloys AA2024 and AA7075. J Alloys Compd 666:493–500. https://doi.org/10.1016/j.jallcom.2016.01.138

29. Padmanaban R, Kishore VR, Balusamy V (2014) Numerical simulation of temperature distribution and material flow during friction stir welding of dissimilar aluminum alloys. Procedia Eng 97:854–863. https://doi.org/10.1016/j.proeng.2014.12.360

30. Song M, Kovacevic R (2004) Heat transfer modelling for both workpiece and tool in the friction stir welding process: a coupled model. Proc Inst Mech Eng Part B J Eng Manuf 218:17–33. https://doi.org/10.1243/095440504772830174

31. Su H, Wu CS, Pittner A, Rethmeier M (2014) Thermal energy generation and distribution in friction stir welding of aluminum alloys. Energy 77:720–731. https://doi.org/10.1016/j.energy.2014.09.045

32. Medhi T, Saha B, Debbarma S, Saha SC (2015) Thermal modelling and effect of process parameters in friction stir welding. Mater Today Proc 2:3178–3187. https://doi.org/10.1016/j.matpr.2015.07.112

33. Zhang Z, Liu YL, Chen JT (2009) Effect of shoulder size on the temperature rise and the material deformation in friction stir welding. Int J Adv Manuf Technol 45:889–895. https://doi.org/10.1007/s00170-009-2034-7

34. Nathan SR, Balasubramanian V, Malarvizhi S, Rao AG (2015) Effect of welding processes on mechanical and microstructural characteristics of high strength low alloy naval grade steel joints. Def Technol 11:308–317. https://doi.org/10.1016/j.dt.2015.06.001

35. Enomoto S (2003) Friction stir welding: research and industrial applications. Weld Int 17:341–345. https://doi.org/10.1533/wint.2003.3114

36. Feng Z, Santella ML, David SA et al (2005) Friction stir spot welding of advanced high-strength steels: a feasibility study. SAE Tech Pap 1:1248. https://doi.org/10.4271/2005-01-1248

37. Yokoyama H, Mitao S, Yamamoto S et al (2001) High strength bainitic steel rails for heavy haul railways with superior damage resistance. NKK Tech Rev 84:44–51

38. Hajizad O, Kumar A, Li Z et al (2019) Influence of microstructure on mechanical properties of bainitic steels in railway applications. Metals (Basel) 9:778. https://doi.org/10.3390/met9070778

39. Prasanna P, Rao BS, Rao GKM (2010) Finite element modeling for maximum temperature in friction stir welding and its validation. Int J Adv Manuf Technol 51:925–933. https://doi.org/10.1007/s00170-010-2693-4

40. Chen CM, Kovacevic R (2003) Finite element modeling of friction stir welding: thermal and thermomechanical analysis. Int J Mach Tools Manuf 43:1319–1326. https://doi.org/10.1016/S0890-6955(03)00158-5

41. Assidi M, Fourment L, Guerdoux S, Nelson T (2010) Friction model for friction stir welding process simulation: calibrations from welding experiments. Int J Mach Tools Manuf 50:143–155. https://doi.org/10.1016/j.ijmachtools.2009.11.008

42. Heurtier P, Jones MJ, Desrayaud C et al (2006) Mechanical and thermal modelling of friction stir welding. J Mater Process Technol 171:348–357. https://doi.org/10.1016/j.jmatprotec.2005.07.014

43. Soundararajan V, Zekovic S, Kovacevic R (2005) Thermo-mechanical model with adaptive boundary conditions for friction stir welding of Al 6061. Int J Mach Tools Manuf 45:1577–1587. https://doi.org/10.1016/j.ijmachtools.2005.02.008

44. Hamilton C, Dymek S, Sommers A (2008) A thermal model of friction stir welding in aluminum alloys. Int J Mach Tools Manuf 48:1120–1130. https://doi.org/10.1016/j.ijmachtools.2008.02.001

45. Schmidt H, Hattel J, Wert J (2004) An analytical model for the heat generation in friction stir welding. Model Simul Mater Sci Eng 12:143–157. https://doi.org/10.1088/0965-0393/12/1/013

46. Kumar R, Singh K, Pandey S (2012) Process forces and heat input as function of process parameters in AA5083 friction stir welds. Trans Nonferrous Met Soc China 22:288–298. https://doi.org/10.1016/S1003-6326(11)61173-4

47. Quintana KJ, Silveira JL (2018) Mechanistic models for the forces in FSW of aluminum alloy 5052-H34. Int J Adv Manuf Technol 96:3993–4008. https://doi.org/10.1007/s00170-018-1859-3

48. Rai R, De A, Bhadeshia HKDH, DebRoy T (2011) Review: friction stir welding tools. Sci Technol Weld Join 16:325–342. https://doi.org/10.1179/1362171811Y.0000000023

49. Niu QL, Zheng XH, Ming WW et al (2013) Friction and wear performance of titanium alloys against tungsten carbide under dry sliding and water lubrication. Tribol Trans 56:101–108. https://doi.org/10.1080/10402004.2012.729296

50. Venkatesh VC, Izman S (2007) Precision engineering, 1st edn. Tata McGraw-Hill Publishing Company Limited, New York

51. Li Q, Pan C, Jiao Y, Hu K (2018) Research on PCBN tool dry cutting GCr15. Machines 28:1–9. https://doi.org/10.3390/machines6030028

52. Meran C, Kovan V, Alptekin A (2007) Friction stir welding of AISI 304 austenitic stainless steel. Materwiss Werksttech 38:829–835. https://doi.org/10.1002/mawe.200700214

53. Das S, Haldar A (2014) Continuously cooled ultrafine bainitic steel with excellent strength-elongation combination. Metall Mater Trans A Phys Metall Mater Sci 45:1844–1854. https://doi.org/10.1007/s11661-013-2173-1

54. Ozlu E, Budak E, Molinari A (2009) Analytical and experimental investigation of rake contact and friction behavior in metal cutting. Int J Mach Tools Manuf 49:865–875. https://doi.org/10.1016/j.ijmachtools.2009.05.005

55. Edwards P, Ramulu M (2010) Peak temperatures during friction stir welding of Ti–6Al–4V. Sci Technol Weld Join 15:468–472. https://doi.org/10.1179/136217110X12665778348425

56. Zhou L, Liu HJ, Liu P, Liu QW (2009) The stir zone microstructure and its formation mechanism in Ti–6Al–4V friction stir welds. Scr Mater 61:596–599. https://doi.org/10.1016/j.scriptamat.2009.05.029

57. Wade M, Reynolds AP (2010) Friction stir weld nugget temperature asymmetry. Sci Technol Weld Join 15:64–69. https://doi.org/10.1179/136217109X12562846839150

58. Cortés VHV, Guerrero GA, Granados IM et al (2019) Effect of retained austenite and non-metallic inclusions on the mechanical properties of resistance spot welding nuggets of low-alloy TRIP steels. Metals (Basel) 9:52–63. https://doi.org/10.3390/met9101064